The stress-pressure relationship in simulations of MRI-induced turbulence

Johnathan Ross[1]⋆, Henrik N. Latter[1], Jerome Guilet[1,2]
[1] *DAMTP, University of Cambridge, CMS, Wilberforce Road, Cambridge CB3 0WA, UK*
[2] *Max-Planck-Institut fur Astrophysik, Karl-Schwarzschild-Str. 1, D-85748 Garching, Germany*

ABSTRACT

We determine how MRI-turbulent stresses depend on gas pressure via a suite of unstratified shearing box simulations. Earlier numerical work reported only a very weak dependence at best, results that call into question the canonical α-disk model and the thermal stability results that follow from it. Our simulations, in contrast, exhibit a stronger relationship, and show that previous work was box-size limited: turbulent 'eddies' were artificially restricted by the numerical domain rather than by the scale height. Zero-net-flux runs without physical diffusion coefficients yield a stress proportional to $P^{0.5}$, where P is pressure. The stresses are also proportional to the grid length and hence remain numerically unconverged. The same runs with physical diffusivities, however, give a result closer to an α-disk: the stress is $\propto P^{0.9}$. Net-flux simulations without explicit diffusion exhibit stresses $\propto P^{0.5}$, but stronger imposed fields weaken this correlation. In summary, compressibility is important for the saturation of the MRI, but the exact stress-pressure relationship is difficult to ascertain in local simulations because of numerical convergence issues and the influence of any imposed flux. As a consequence, the interpretation of thermal stability behaviour in local simulations is a problematic enterprise.

Key words: accretion, accretion disks — MHD — turbulence

1 INTRODUCTION

The accretion of gas through a disk, and ultimately on to a star or black hole, powers the intense luminosity of a great many astrophysical objects. The classical theory of disk accretion assumes that (a) correlated turbulent motions in the disk apply a torque that drives the observed transport, and that (b) the resulting radial-azimuthal component of the stress $\Pi_{r\phi}$ is proportional to the gas pressure P, i.e. $\Pi_{r\phi} = \alpha P$ (Lynden-Bell & Pringle 1973, Shakura & Sunyaev 1973). This model permits the closure of the system of governing equations, allowing researchers to construct disk solutions with which to interpret observations.

At present the consensus is that the magnetorotational instability (MRI) generates disk turbulence, at least in disks that are sufficiently ionised (Balbus & Hawley 1991, 1998). Numerical simulations of the MRI in unstratified local domains certainly yield appropriate values for α in cases where the computational domain is penetrated by a strong magnetic field (Hawley et al. 1995, Simon et al. 2009). In contrast to the measurement of α, however, there have been relatively few attempts to test whether $\Pi_{r\phi}$ is in fact proportional to

P. Four studies exist: Hawley et al. (1995, hereafter HGB95), Sano et al. (2004, SITS04), Simon et al. (2009, SHB09) and most recently Minoshima et al. (2015, MHS15) which appeared when this paper was in draft form. All four were undertaken in unstratified shearing boxes, and show that $\Pi_{r\phi}$ depends on P to a very weak power or not at all (see also Blackman et al. 2008). Taken on face value, these results imply that the MRI saturates with little or no recourse to compressibility, and moreover cast doubt on the validity of the α-model, and the many structure and stability results that issue from it.

In this paper, we re-examine the relationship between the MRI-induced turbulent stress and the gas pressure with numerical simulations in local unstratified boxes. We employ the codes Ramses (Teyssier 2002, Fromang et al. 2006). In our main runs the gas is permitted to heat up, via turbulent dissipation, and we compare the correlation between $\Pi_{r\phi}$ and P during this phase. Special care has been taken to minimise the influence of the box size on our results, and so we have set $H < L$ in most runs, where H is the 'scale height' (the characteristic distance travelled by a sound wave over one orbit) and L is the vertical and radial box lengths. This is key. In the opposite regime, $H > L$, the turbulent eddies are always limited by the box (a numerical effect) and not

⋆ E-mail: jpjr2@cam.ac.uk

by compressibility (a physical effect). As a consequence, the relationship between MRI saturation and compressibility is lost. Note that the previous simulations of HGB95, SITS04, SHB09, and MHS15 almost always use $H > L$, and hence suffer from this shortcoming.

Runs with $L \geqslant 2H$, yield a $\Pi_{r\phi}$ that depends on P in a stronger way than in earlier work. When there is no net magnetic flux and no explicit diffusion coefficients, we obtain $\Pi_{r\phi} \propto P^q$ with $q \approx 0.4-0.6$ in both heating and cooling runs. In fact, the simulations indicate that $\Pi_{r\phi} \sim H\Delta$, where Δ is the grid length. This result shows that the stress is unconverged with respect to the numerical parameters — a pathology of this particular set-up (see also Fromang & Papaloizou 2007). A suite of isothermal simulations of differing box sizes and differing resolutions confirms this basic idea. The incorporation of physical diffusivities, however, elicits strikingly different behaviour: the stress and pressure are then almost proportional, with $q \approx 0.9$. On the other hand, both net-toroidal and net-vertical flux simulations yield $q \approx 0.2 - 0.5$. In these cases q depends on the strength of the background magnetic field. The stronger the imposed flux, the weaker the correlation between $\Pi_{r\phi}$ and P.

Despite these various complications, we have demonstrated that compressibility is important in the saturation of the MRI. The exact form of the stress-pressure relationship, however, is difficult to extract from local simulations because of the issue of numerical convergence and the strength of any imposed flux. This makes local simulations of thermal stability particularly difficult to interpret.

The structure of the paper is as follows. In the next two sections we outline a very basic theoretical framework with which to interpret our results, and then give details of the numerical model and methods with which we attack the problem. Our results appear in Sections 4 and 5, which treat zero-net-flux and net-flux configurations separately. We bring everything together in Section 6 and discuss implications for the saturation of the MRI and the possibility of thermal instability.

2   THEORETICAL EXPECTATIONS

In this section we restate the heuristic, and essentially hydrodynamical, arguments that justify the α-prescription. We then show how an insufficiently large box impinges on the stress's dependence on P. Finally, we speculate on how the presence of magnetic fields may change this picture.

2.1   Hydrodynamical arguments

Our initial assumption is that shear turbulence will act so as to eradicate the destabilising conditions from which it sprung. In other words, it will transport as much angular momentum outward as is possible. We next assume that the only restriction on the efficiency of this transport comes from the finite thickness of the disk and from compressibility: turbulent eddies cannot be larger than H, and turbulent speeds cannot exceed the sound speed c_s. If the motions were faster, enhanced dissipation from shocks would slow them till they were subsonic. In order to maximise transport, however, the turbulence will induce flows as close to c_s as it can. Note that

we are assuming there is not a more stringent restriction, arising from a separate incompressible mechanism, that limits the turbulence to shorter scales. Consequently, we may write

$$\Pi_{r\phi} \sim \rho \, v_r v_\phi \sim \rho \left(l_{\mathrm{turb}} \Omega\right)^2,$$

where v_r and v_ϕ are the characteristic radial and azimuthal speeds of the largest eddies, and l_{turb} is their characteristic size. Letting either $v \lesssim c_s$ or $l_{\mathrm{turb}} \lesssim H$ yields the alpha prescription, and we have $\Pi_{r\phi} = \alpha P$, for some constant $\alpha < 1$. In terms of the scale height, $\Pi_{r\phi} \sim H^2$.

An alternative argument uses dimensional analysis, a version of which we now briefly give. Imagine a 'perfect' shearing box simulation, perfect in the sense that its outcome is independent of the numerical domain size or the small scales. There are three relevant physical quantities, $\Pi_{r\phi}$, c_s, ρ (whose dependence on time is implicit), and two physical dimensions, mass density, and speed. There is hence only one way to relate these quantities, $\Pi_{r\phi} \propto \rho c_s^2$, and we arrive at the alpha model once again[1].

2.2   Box-size limitations

Consider numerical simulations performed in unstratified boxes with a vertical and radial size of L. If $L \gg H$, then the computational domain should play a negligible role, and the above argument will hold: $\Pi_{r\phi} \sim H^2$. If, on the other hand, $L \ll H$ then the turbulent eddies will be limited not by H but by L. With $l_{\mathrm{eddy}} \lesssim L$, one obtains $\Pi_{r\phi} \sim L^2$, and the stress becomes a constant, independent of H (and hence P). This could be considered the 'incompressible limit'. When $L \sim H$ these two limits should smoothly join up, and in Fig. 1 we provide a sketch showing how this might look.

The simulations of HGB95, SITS04 and SHB09 allow the box to heat up due to turbulent dissipation. Hence the scale height H increases monotonically over time, reaching values, in some cases, many orders of magnitude greater than its starting value H_0. In Fig. 1 we may treat H^2 as a proxy for time, with the evolution of the stress following the blue curve to the right, rising with H and then plateauing once the eddies hit the box size. Importantly, $H_0 > L$ in all the SHB09 runs and in all but a handful of the SITS04 and MHS15 runs. Thus their simulations' initial states fall mainly to the right of the red dot in Fig. 1. This means that the stress's evolution is strongly constrained by the box, capable of increasing marginally, if at all. As a consequence, these studies are unable to truly test how strongly $\Pi_{r\phi}$ depends on P.

To remove the artificial effect of the box size we must begin to the left of the red dot, ideally to the left of the red star. The main aim of this paper is to present runs with initial states as deep into this regime as possible.
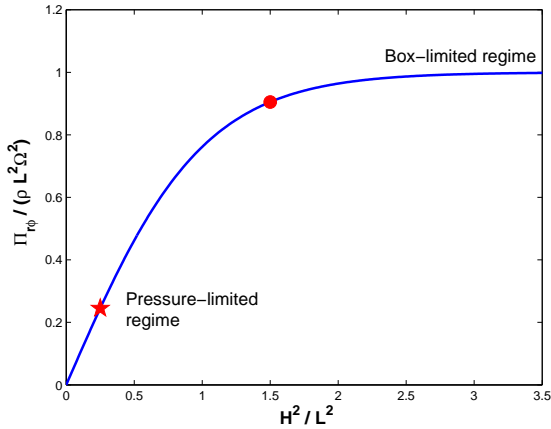
Figure 1. A schematic graph of how we expect the stress $\Pi_{r\phi}$ to depend on scale height H in an unstratified MRI simulation with a box size of L. In monotonically heating runs the stress will evolve by following the blue curve from left to right. Very roughly, the box-limited regime is to the right of the red dot, whereas the pressure-limited regime is to the left of the red star. Ideally, simulations should begin to the left of the red star.

2.3 Magnetohydrodynamical complications

MRI turbulence involves magnetic fields, obviously, which we expect to spoil this attractively simple picture. For starters, simulations without a net flux highlight the smallest scales over the largest. In the absence of physical diffusivities, the characteristic eddy scale l_{turb} prefers to sit near the fixed grid scale Δ, and as a result simulations return $\Pi_{r\phi} \propto \Delta$ (Fromang & Papaloizou 2007, Simon et al. 2009). This dependence of the stress on Δ may partly wash out the dependence on H.

When physical diffusivities are incorporated the situation is not much improved: the ensuing turbulent dynamo depends on the magnetic Prandtl number, and thus on the (fixed) small scales (Fromang et al. 2007, Riols et al. 2013, 2015). Having said that, large-scales are not completely irrelevant. In boxes of different aspect ratios the dynamo exhibits long term oscillations with coherent magnetic field reversals on the box size (Lesur & Ogilvie 2008a, b). Evidently, the dynamics are complicated and may involve interactions between multiple scales. Certainly, the stress-pressure relationship could differ from the picture described in Section 2.1.

On the other hand, simulations involving a net flux witness the excitation of large-scale coherent motions, such as channel flows. Our simple picture of transport via turbulent eddies may be complicated by these features, which periodically emerge from the turbulent melee and dominate the angular momentum transport (HGB95, Inutsuka & Sano 2001, Bodo et al. 2008, SHB09). Compressibility fails to limit the development of channel flows, instead concentrating them into thin jets and current sheets (Latter et al. 2009, Lesaffre et al. 2009). If these flows dominate $\Pi_{r\phi}$ it is likely that the H dependence explored above is muddled or completely lost.

More generally, turbulent transport in MHD is dominated by an anisotropic tangle of flux linkages which take time to develop and also to destroy. How these magnetic structures respond as the pressure rises and falls is unclear, but appreciable time lags may build up between the variations in pressure and in magnetic transport, involving no doubt the efficiency of magnetic reconnection. As a consequence, the relationship between stress and pressure may not be a simple power law, but may include memory effects, for example (cf. Ogilvie 2003, Pessah et al. 2006).

Though not an MHD effect per se, but one that relates to time lags, is the issue of causation: is P driving $\Pi_{r\phi}$ or vice versa? Section 2.1 argues that as pressure increases, the stress follows. But a variation in stress can also force a change in the temperature (and hence pressure) due to its associated variation in dissipation (see arguments in Hirose et al. 2009). Though this interdependence is undoubtedly a complication, the timescales of the two processes differ and can be partly separated; the stress's action on the pressure occurs on shorter timescales than the pressure's action on the stress (Latter & Papaloizou 2012).

We have flagged quite a number of issues in this subsection, mainly for reference. In practice, not all directly impinge on our results. In what follows we explore primarily the significance of the small scales and the strength of any net flux. But before we show our results we present the details of our physical model and numerical set-up.

3 GOVERNING EQUATIONS AND NUMERICAL SET UP

In this paper we solve the equations of compressible MHD in the unstratified shearing box approximation (Goldreich and Lynden-Bell 1965). It uses a local Cartesian frame of reference which is corotating with a Keplerian disk at some arbitrary radius, R_0, with angular frequency $\boldsymbol{\Omega} = \Omega \hat{\boldsymbol{e}}_z$. As is conventional, $\hat{\boldsymbol{e}}_x$, $\hat{\boldsymbol{e}}_y$, $\hat{\boldsymbol{e}}_z$ are taken to be the unit vectors in the radial, azimuthal and vertical directions respectively. In this frame of reference, the equations of motion can be written as

$$\frac{\partial \rho}{\partial t} + \nabla \cdot (\rho \boldsymbol{v}) = 0, \tag{1}$$

$$\rho \frac{\partial \boldsymbol{v}}{\partial t} + \rho(\boldsymbol{v} \cdot \nabla)\boldsymbol{v} = -2\rho \boldsymbol{\Omega} \times \mathbf{v} + 3\rho\Omega^2 \hat{\boldsymbol{e}}_x - \nabla P$$
$$+ (\nabla \times \boldsymbol{B}) \times \boldsymbol{B} + \nabla \cdot \mathbf{T}, \tag{2}$$

$$\frac{\partial \boldsymbol{B}}{\partial t} = \nabla \times (\boldsymbol{v} \times \boldsymbol{B}) + \eta \nabla^2 \boldsymbol{B}, \tag{3}$$

where ρ is the mass density, $\boldsymbol{v}$ is the velocity, P is the gas pressure $\boldsymbol{B}$ is the magnetic field, and η is the magnetic diffusivity. The (molecular) viscous stress is given by $\mathbf{T} = \nu(\nabla \boldsymbol{v} + \nabla \boldsymbol{v}^T)$, with ν the shear viscosity. In most runs, $\nu = \eta = 0$.

We adopt either an isothermal or an ideal gas equation of state. In the former

$$P = \rho c_0^2, \tag{4}$$

where c_0 is the fixed isothermal sound speed. Otherwise, we must solve for the internal energy ε,

$$\frac{\partial \varepsilon}{\partial t} + \boldsymbol{v} \cdot \nabla \varepsilon = -P \nabla \cdot \boldsymbol{v} + Q - \Lambda, \tag{5}$$

where $Q = \rho\nu |\nabla \times \boldsymbol{v}|^2 + \eta |\nabla \times \boldsymbol{B}|^2$ is the sum of the viscous

heating and the resistive heating and Λ is a cooling function. For an ideal gas

$$\varepsilon = P/(\gamma - 1), \qquad (6)$$

where γ is the adiabatic index. We typically take $\gamma = 7/5$. In non-isothermal runs, the sound speed is then given by $c_s = (\gamma P/\rho)^{1/2}$ and the pressure scale height by $H = (2/\gamma)^{1/2} c_s/\Omega$. Finally, when non-zero, the cooling law is usually

$$\Lambda = \theta\, P^m, \qquad (7)$$

where θ and m are constants. Some runs, however, set Λ to be some fixed fraction of the dissipated energy.

3.1   Numerical methods

The set of equations just described are solved using Ramses, a finite volume code based on the MUSCL-Hancock algorithm (Teyssier 2002; Fromang et al. 2006). Our version of the code solves the shearing box equations on a uniform grid, and has been tested with an isothermal equation of state in Fromang & Stone (2009), Latter et al. (2010) and Fromang et al. (2013).

Instead of the total y-momentum equation, we evolve the equivalent conservation law for the angular momentum fluctuation $\rho v'_y = \rho(v_y - v_K)$, with v_K the Keplerian velocity. The azimuthal advection arising from v_K is solved using an upwind solver. Shearing box source terms in the momentum equation (due to tidal gravity and Coriolis forces) are implemented following the Crank-Nicholson algorithm described in Stone & Gardiner (2010).

The algorithm solves for the fluctuation energy $E' \equiv P/(\gamma - 1) + \rho v'^2/2 + B^2/2$. In the absence of explicit dissipation, its conservation law is written as

$$\frac{\partial E'}{\partial t} + \nabla \cdot \left(E'\boldsymbol{v}' + \boldsymbol{v}' \cdot \mathbf{P}\right) = -v_K \frac{\partial E'}{\partial y} + \left(B_x B_y - \rho v_x v'_y\right)\frac{\partial v_K}{\partial x}, \qquad (8)$$

where $\mathbf{P}$ is the total pressure tensor

$$\mathbf{P} = (P + B^2/2)\mathbf{I} - \boldsymbol{BB}. \qquad (9)$$

The left hand side Eq. (8) is the usual energy conservation law, which we solve using the MUSCL-Hancock algorithm. The treatment of the two terms on the right hand have been modified: the azimuthal advection of energy is solved with an upwind solver, and the second term involving the Maxwell and Reynolds stresses is added as a source term. Several numerical tests of this implementation are presented in Appendix A. The simulations presented in this paper used the HLLD Riemann solver (Miyoshi & Kusano 2005), and the multidimensional slope limiter described in Suresh (2000).

3.2   Parameters and initial conditions

We adopt the same units as HGB95, so that $\Omega = 10^{-3}$, the initial density is $\rho_0 = 1$, and the initial sound speed $c_{s0} = 10^{-3}$ in diabatic runs, or $c_0 = 10^{-3}$ in isothermal runs. Thus the initial scale height is $H_0 = 1$, though often we retain the notation explicitly for clarity. Note that, in contrast, H is a function of P and thus changes in thermally evolving simulations, increasing as the box heats up, and

decreasing as it cools down. Finally, we denote by $T_{\rm orb}$ the period of one orbit.

Three initial configurations of magnetic field are considered: (a) zero net-flux, for which $\boldsymbol{B} = B_0 \sin(2\pi x)\hat{\boldsymbol{e}}_z$, (b) net-toroidal flux, $\boldsymbol{B} = B_0\hat{\boldsymbol{e}}_y$, and (c) net-vertical flux, $\boldsymbol{B} = B_0\hat{\boldsymbol{e}}_z$. We define a plasma beta in code units through $\beta = 2/B_0^2$, which we set to 10^3 unless otherwise stated. To induce the MRI we introduce random velocity perturbations in all principle directions with amplitudes $< 0.1c_{s0}$.

Typically the radial and vertical sizes of the computational domain (L_x and L_z) are the same and denoted by L, some multiple of H_0. The azimuthal size is $L_y = 5H_0$. Unless otherwise stated, the resolution for the thermally evolving simulations is $\Delta = H_0/N = 1/64$, and is the same in all directions.

Physical diffusion is neglected in all but a handful of zero-net-flux simulations for which $\nu = 8 \times 10^{-7}$ and $\eta = 2 \times 10^{-7}$. These values correspond to a magnetic Prandtl number of $P_m = \nu/\eta = 4$, and Reynolds and magnetic Reynolds numbers of $Re \equiv H_0 c_{s0}/\nu = 1250$ and $R_m \equiv H_0 c_{s0}/\eta = 5000$. These guarantee sustained turbulence and converged results (Fromang 2010).

3.3   Diagnostics

The transport of angular momentum is dictated by the turbulent stress which is given by the sum of the Reynolds and Maxwell stresses

$$\Pi_{xy} = -B_x B_y + \rho v_x v'_y. \qquad (10)$$

It is the behaviour of this quantity as P varies that we are most interested in. During diabatic simulations we calculate $\langle \Pi_{xy}\rangle/P_0$, where the angled brackets indicate an instantaneous box average and P_0 is the initial pressure. In isothermal simulations we are interested in the time and box averaged rate of angular momentum transport, which corresponds to the usual definition of the alpha parameter:

$$\alpha = \langle\langle \Pi_{xy}\rangle\rangle/P_0. \qquad (11)$$

The double angle brackets represent averages over both volume and time, the latter taken once we judge the system to have entered its saturated state.

In order to quantify the relationship between Π_{xy} and P we assume that

$$\Pi_{xy} \propto P^q, \qquad (12)$$

for some number q which we must determine. In heating runs, the pressure increases monotonically, while the stress increases for some period of time and then plateaus once the box size intervenes (in accord with Fig. 1). By plotting the log of Π_{xy} versus the log of P during the growth phase we may obtain q. Unfortunately, the calculation of q is not unambiguous. The stress is often bursty and the time of the growth phase relatively short. We hence can only give a rough estimate for q.

Finally, a useful diagnostic used by Lesur and Longaretti (2007) is the vertical correlation length. We define

this correlation length by

$$\zeta_z(v_z) =$$

$$\left\langle\left\langle \frac{\int\int v_z(x, y = L_y/2, z)v_z(x, y = L_y/2, z')dz'dz}{\int v_z^2(x, y = L_y/2, z)dz} \right\rangle\right\rangle_{T_{orb}}$$
(13)

where the inner angled brackets represent an average over the x direction and the outer angles brackets signify an average over 1 orbit.

4 ZERO-NET-FLUX SIMULATIONS

We cover the three possible topologies of the magnetic field in two separate sections, starting with zero-net flux. First we present our main results which display the effect of increased gas pressure on the stress, and how the box size and the diffusion scales impact on this behaviour. Cooling runs are presented next, where a similar dependence is observed. Finally, we look at isothermal simulations of differing sizes to see if these trends are reproduced in simulations that are in quasi-equilibrium. We place additional tests in Appendix B that reinforce our results.

4.1 Heating runs

4.1.1 Influence of the box size

We start off by considering boxes with no cooling ($\Lambda = 0$) and no explicit diffusion ($\nu = \eta = 0$). The simulations, however, heat up by numerical dissipation which is captured by our total energy conserving scheme. We examine boxes with radial and vertical extents of $L = H_0$, $2H_0$, and $4H_0$, all with $\Delta = H_0/64$.

The time histories of the pressure and stress of the $L = 4H_0$ simulation may be viewed in Fig. 2. While the pressure shows the monotonic increase expected, the stress's evolution is more complicated. First, it undergoes an exponential growth, corresponding to the onset of the linear instability, followed by a rapid decrease in stress as the initially ordered flow breaks down into turbulence. This phase only takes a handful of orbits. For the next 60 orbits, the stress exhibits significant growth, of almost a factor of 3. During the same phase, the pressure has increased by a factor of about 5. After 60 orbits the system enters a third phase: the pressure carries on growing but the stress plateaus and suffers large amplitude bursts (in contrast to the more placid earlier stages). In summary, the system, adheres rather closely to the expectations outlined in Section 2.2: after the linear phase, the box heats up, with the stress following behind, but once the turbulent eddy sizes hit the box size they can grow no more and the stress reaches a constant level.

In Fig. 3 we plot the stress as a function of pressure, in order to estimate q. As mentioned earlier, this is not without ambiguity and we overplot lines of $q = 0.5$ and $q = 0.7$ to indicate possible ranges for this quantity. Despite the uncertainty it is clear that, before the box size interferes, there is a relatively strong correlation between P and Π_{xy}. This is in marked contrast to earlier work.

As argued in Section 2, we believe that previous simulations gave lower qs as a result of insufficiently large boxes. To
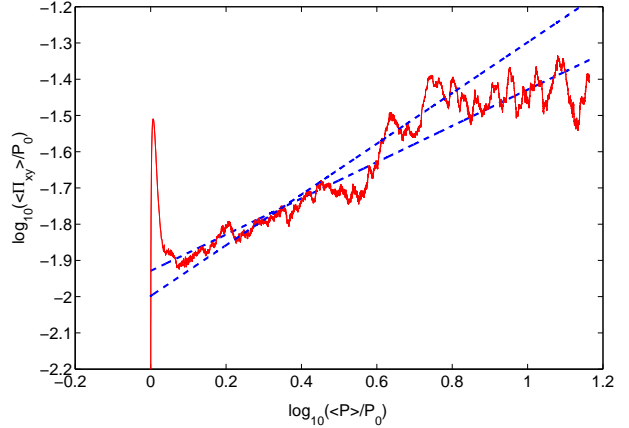
Figure 3. The time evolution of the stress normalized by the initial gas pressure, as a function of the volume averaged pressure for a $L = 4H_0$ simulation (red solid curve). The blue dashed lines have slopes 0.5 and 0.7.

test this idea, we ran simulations with smaller L. The results are shown in Fig. 4. For $L = H_0$, we obtain only a minimal increase of stress with pressure. We find that $q = 0.1 - 0.3$ which is consistent with the $q = 0.25$ achieved by SITS04, who used similarly sized boxes. The q increases when we move to $L = 2H_0$. We find then that $q = 0.4 - 0.6$. Though the determination of q is made difficult by the enhanced burstiness of the signal, the result is clear: the H_0 box is too small to adequately describe the growth of the stress. In addition, the fact that $q \approx 0.5$ in both the $2H_0$ and $4H_0$ boxes suggests that q has converged with respect to L in the $2H_0$ box.

4.1.2 Influence of the grid

It must be emphasised that the result $q \approx 0.5$ is still very much determined by the numerical parameters. On dimensional grounds (cf. Section 2.1), any deviation from $q = 1$ *must* arise from either a dependence on the box size, on the grid scale, or on both. In the previous subsection we investigated the influence of L, in this subsection we investigate Δ.

Fromang & Papaloizou (2007) found that the stress is proportional to the grid scale Δ in their isothermal simulations. Suppressing the box size dependence for the moment, these results suggest the scaling $\Pi_{xy} \sim \rho\Delta\Omega c_s \sim P^{1/2}$ in agreement with the $q \approx 0.5$ we find. To reproduce this scaling in our heating runs we took the $L = 2H_0$ box and tried resolutions of $\Delta = H_0/16$, $H_0/32$, in addition to the fiducial $H_0/64$. In all cases $q \approx 0.5$. In addition, during both the growth phase and the plateau phase, the magnitude of the stresses is proportional to Δ, with the stress plateau taking values ≈ 0.12, 0.063, and 0.03 for the three Δs tried.

In summary, this sequence suggests that the stress scales as

$$\Pi_{xy} \sim \rho\Delta\Omega c_s, \qquad (14)$$

during the first stages of the simulation (when the influence of the box size is mitigated). Afterwards it scales as

$$\Pi_{xy} \sim \rho\Delta L\Omega^2, \qquad (15)$$
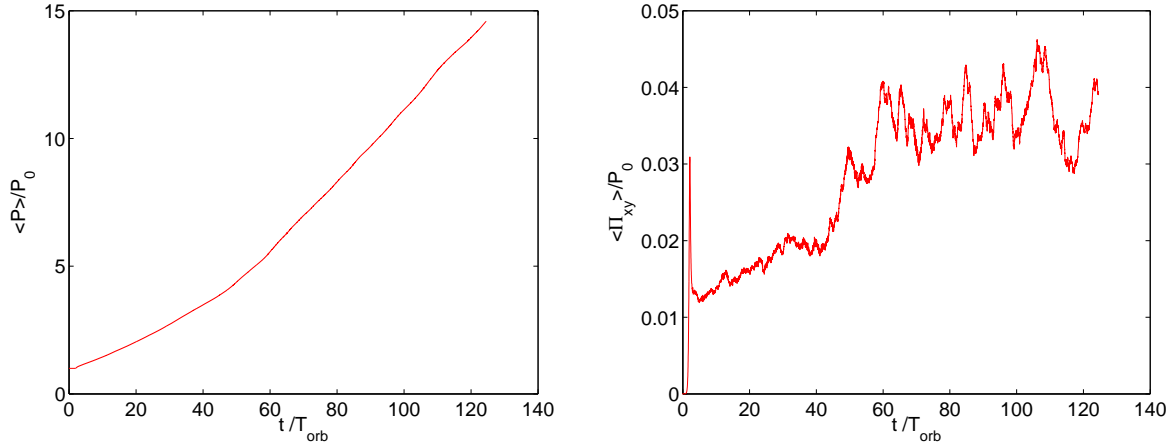
Figure 2. The time evolution of the gas pressure P (left panel) and the total stress normalized by the initial gas pressure (right panel) for the zero-net-flux $L = 4H_0$ simulation.

during the plateau stage, once H grows sufficiently large.

Certainly, these results do not meet all the predictions of Sections 2.1 and 2.2. Though q increases in larger boxes, it does not approach the value 1. Moreover, the maximum stresses achieved are too small, proportional to L not L^2. Obviously, the grid is obstructing the growth of the stress, preventing it from (a) fully responding to the pressure and (b) from obtaining larger values. As first shown by Fromang & Papaloizou (2007), MRI turbulence prefers to anchor itself on the grid scale, and this imposes a constraint comparable to that enforced by the acoustic radiation. In fact, if the fluid velocities follow c_s but the turbulent lengthscales are stuck on the grid, so that $l_{\mathrm{turb}} \sim \Delta$, then we obtain the simulated result $q \approx 0.5$.

To test this idea we calculate the correlation length for the $4H_0$ box and plot the outcome in Fig. 5. If l_{turb} was stuck on the grid then the correlation length would stay constant with time. Actually, the figure reveals a modest increase. Over 60 orbits this is some ≈ 1.4, after which $\zeta_z(v_z)$ plateaus. Considering that the stress only grows by a factor 3, the increase in $\zeta_z(v_z)$ is not negligible and reveals that the correlation length is not entirely anchored to Δ, though it cannot wander too far away.

In conclusion, these results indicate that it may be impossible to obtain numerical convergence when determining the stress-pressure relationship in zero-flux simulations of this type. Though the influence of the box size may be mitigated to some extent, the influence of the grid size is fundamental and cannot be escaped. The stress is proportional to Δ, which forces $q = 0.5$ on dimensional grounds. This problem potentially limits the application of the simulations to physical situations.

4.1.3   Influence of physical diffusion

In order to further probe what the small scales are doing, we undertook simulations with explicit diffusion coefficients. Fromang (2010) found that, in isothermal runs, the stress is approximately independent of the Reynolds number for $P_m = 4$ when Re takes values between $Re = 3125$ and 12500. This suggests that the influence of the physical diffusion
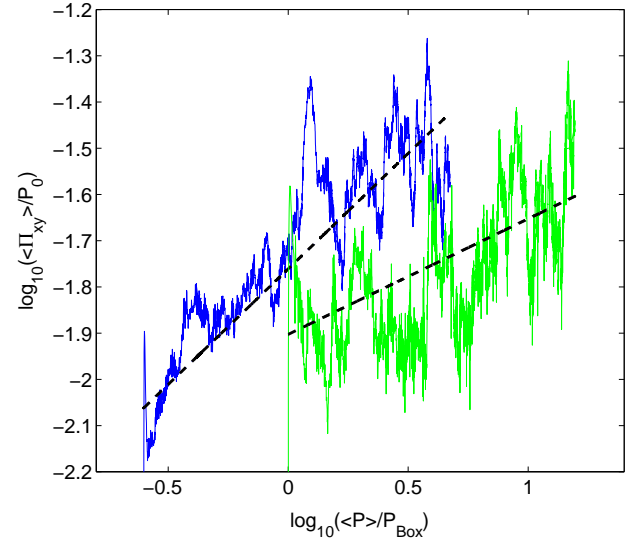

Figure 4. The time evolution of the total stress against the gas pressure normalized by $P_{Box} = P_0 L^2 / H_0^2$. The blue curve is from the $L = 2H_0$ simulation and the green curve is from the $L = H_0$ simulation. Lines with slopes 0.25 and 0.5 are included for comparison.

scales (as opposed to the numerical diffusion scales) may disappear if they are forced to be sufficiently small.

To test this we adopt boxes of size H_0, $2H_0$ and $4H_0$ with $Re = 1250$ and $Rm = 5000$. When $\Delta = H_0/64$, the resistive scale is resolved and the viscous scale is marginally resolved (see Appendix B for more details). As in the previous subsection, we find that when the box size increases so to does q: from ≈ 0, to 0.5, and finally to 0.9 in the largest box. The time evolution of stress against P is plotted in Fig. 6 (red curve) for the $4H_0$ box. For comparison we have overplotted the curve of the diffusionless $4H_0$ run (blue curve).

The most striking result, of course, is that in sufficiently large boxes q can achieve a value close to 1, which is more in line with our initial expectations. In addition, the stress
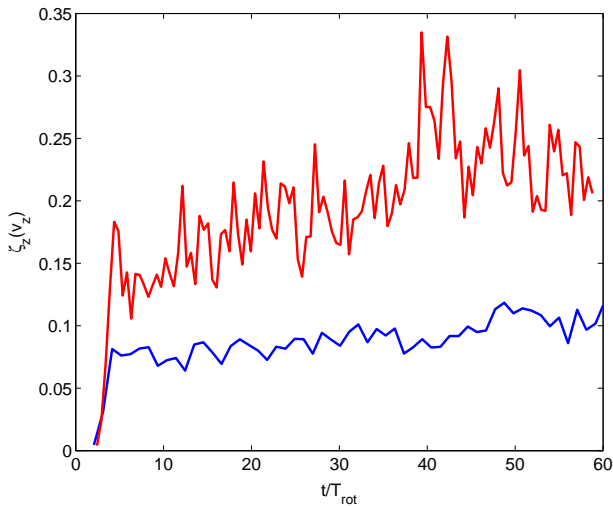
Figure 5. The time evolution of the correlation length, defined in Eq. (13), for the $L = 4H_0$ simulation without physical diffusivities (blue curve), and the $L = 4H_0$ simulation with physical diffusivities (red curve).
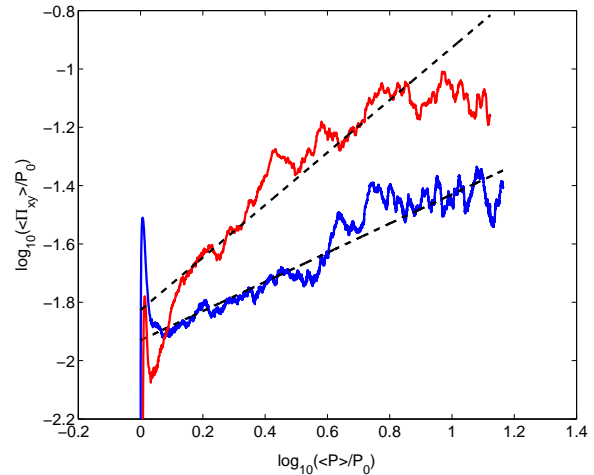

Figure 6. The time evolution of the total stress normalized by the initial gas pressure, as a function of the volume averaged pressure for $L = 4H_0$ simulations. The red curve is from a simulation with explicit diffusivities. The blue curve is from a simulation identical in all respects other than that explicit diffusivities are omitted. Lines of slopes 0.5 and 0.9 have been superimposed for clarity.

increases to larger values than earlier. Physical diffusion elicits dramatically different behaviour vis-a-vis the numerical grid. It would appear that the former does not constrain the turbulent eddies nearly so forcefully, leading to a stress that can grow more freely. In Fig. 5 the correlation length is plotted, which further illustrates the contrast between the two cases.

The reason for why q is not exactly 1 may be due to the residual influence of the box, or possibly the influence of the Reynolds numbers. The fact that the viscous scales are only marginally resolved could also play a role. But note that the stress only increases by a factor of some 5 before it plateaus, not the factor 16 we might expect if l_{turb} increased from H_0 to $4H_0$. The reason seems to be that the plateau phase starts before H reaches the box size, such that H increases by a factor only ~ 2.5 during the growth phase of the stress, and not the anticipated factor 4 (Fig. 6). Simulations with yet bigger boxes as well as higher Re and Rm, though numerically expensive, could help better understand what is going on here. For the moment we limit ourselves to emphasising the striking difference between the case with explicit diffusion and the case without. The former exhibits a stress-pressure relationship much closer to the standard alpha model, and moreover has the potential to give converged answers with respect to the numerical parameters.

4.2 Cooling runs

So far we have captured the stress-pressure relationship by heating up the system (increasing P) and seeing what happens to the stress. A complementary approach is to observe the stresses as the system cools (i.e. as P decreases). If there truly is a meaningful correlation between the two, then the stress must increase and decrease at the same rate in the two cases.

We take a $L = 4H_0$ box with lower resolution $\Delta = H_0/32$, no physical diffusivities, and initially impose no cool-

ing. The fluid heats up until the thermal pressure increases by over an order of magnitude and $H \approx L = 4H_0$. At this point, we introduce a cooling law with $m = 2$ and θ chosen to introduce a stable thermal fixed point at $P \sim P_0$, i.e. $H = H_0$. The fluid is then attracted to this cooler state. The ensuing cooling phase of the simulation is plotted in Fig. 7.

Unlike the heating evolution, described in Fig. 3, the system evolves from the top right to the bottom left but in most other respects shares the same shape and importantly the same q. Once the system cools to the point that $P \approx 5P_0$, the plateau stage ends, and the stress starts decreasing. The main difference is that Π_{xy} is systematically larger in the cooling run as compared to the earlier heating run; but this is due entirely to the lower resolution used (see previous subsection). Also at the end of the cooling phase, when H is small, the turbulence becomes unusually bursty. This is due possibly to the increased proximity of the system to criticality (H is closer to Δ).

4.3 Isothermal runs

In the previous subsections we described the stress-pressure relationship in systems out of equilibrium. Following SITS04 and Pessah et al. (2007), we can also look at isothermal systems that have reached a quasi-equilibrium and observe how the saturated stress depends on the scales L, H and Δ. As emphasised earlier, previous simulations use $L \lesssim H$ and are in the box-dominated regime. We look at isothermal simulations in the opposite limit, with a suite of simulations of fixed H but of $L = H$, $(3/2)H$, $2H$, $4H$, and $8H$.

First, we hold the resolution fixed per L, which means the resolution per H varies from run to run. This scenario mimics the heating runs in Section 4.1 where, as the box heats up and H grows, the number of grid zones per H increases. The αs computed are listed in Table I, where the rough scaling $\alpha \sim L/H$ is exhibited, significantly weaker
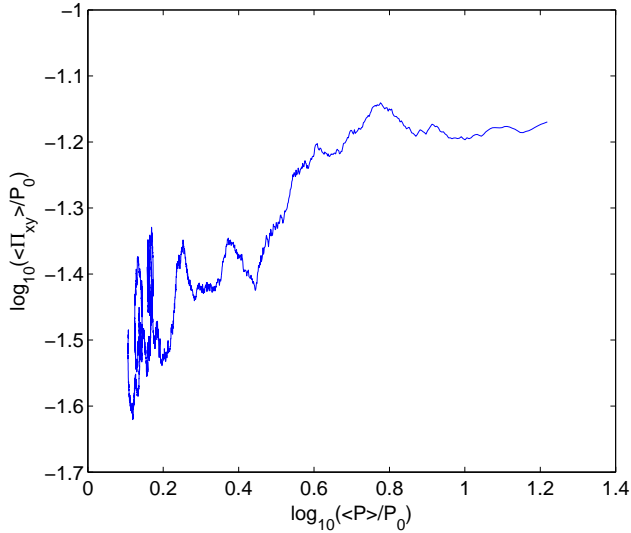
Figure 7. The time evolution of the total stress normalized by the initial gas pressure, as a function of the volume averaged pressure for a $L = 4H_0$ simulation (blue solid curve) when a constant cooling is introduced. Note that the system evolves from right to left. This should be compared to the analogous heating run in Fig. 3.

L/H	Δ/H	α	Type
1	1/64	0.0110	ZNF
3/2	3/128	0.0159	ZNF
2	1/32	0.0199	ZNF
1	1/32	0.0137	ZNF
2	1/32	0.0199	ZNF
4	1/32	0.0246	ZNF
8	1/32	0.0301	ZNF
1	1/32	0.0154	Tor
2	1/32	0.0214	Tor
4	1/32	0.0287	Tor

Table I. The average α for isothermal simulations with varying L and Δ. The two field configurations are zero-net-vertical flux ('ZNF') and net toroidal flux ('Tor'), the latter employs $\beta = 1000$.

than Pessah et al. (2007), who find $\alpha \sim (L/H)^{5/3}$. This we attribute to the fact that $L > H$.

The turbulent α must also be proportional to a dimensionless function of the ratio L/Δ. In order to determine this function, we undertake a set of simulations exploring a larger range of box sizes and with the number of grid points per H remaining constant. The calculated αs are listed in Table I and plotted as a function of L/H in Fig. 8. Now we find the rough scaling $\alpha \sim (L/H)^{2/5}$. Combining the two scalings from the two sequences of runs yields an expression for the stress

$$\Pi_{xy} \sim \rho H \Delta^{3/5} L^{2/5} \Omega^2, \tag{16}$$

which holds for isothermal simulations in which $H < L$.

Estimate (16) raises a number of points. First, it implies that $\Pi_{xy} \sim P^{1/2}$, yielding a q in agreement with our heating runs of Section 4.1, a cross-validation that inspires confidence in both results. Second, the stress is $\sim \Delta^{3/5}$, in contrast to Fromang & Papaloizou (2007) and Pessah
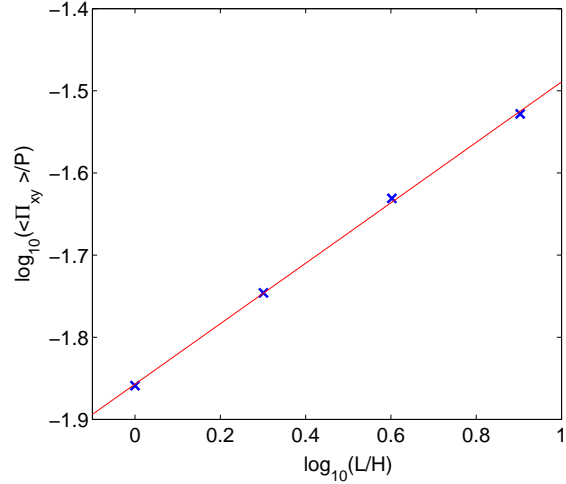
Figure 8. Total stress, normalised by the pressure, as a function of the ratio of the box size to scale height for isothermal zero-net-flux simulations. For comparison, a curve with $\alpha \propto (L/H_0)^{0.37}$ is overlaid.

et al. (2007), who find it proportional to Δ. This puzzling disagreement could be due to the fact that our simulations are in the $L > H$ regime, or it could perhaps issue from different box aspect ratios. Certainly the discrepancy encourages further work. Third, the system cannot escape the influence of the box size, even in the largest of the simulations. We expected that when $L = 8H$ there would be a separation of scales between L and l_{turb} (whether the latter is set by H or Δ) and that the turbulent eddies might no longer feel L. This is evidently not the case. It suggests that large-scale structures, magnetic or acoustic, play some role even in zero-net-flux turbulence (see also Guan et al. 2009, hereafter GGSG09). These structures can develop because the simulation has been run for a long time (in order to reach equilibrium) and the box has begun to 'sense' its finite size and its periodicity. This is probably not the case in the heating runs of Section 4.1, and one might conclude that isothermal (or any long-time equilibrium) simulations are inappropriate for determining the instantaneous stress-pressure relationship.

5 NET-FLUX SIMULATIONS

5.1 Toroidal fields

We now examine the effect of the vertical box size on the stress-pressure relationship in net-toroidal field simulations. Explicit diffusion coefficients are omitted, but the boxes are permitted to heat up via numerical dissipation. We use, $\Delta = H_0/32$ and set $L = H_0$, $2H_0$, and $4H_0$. The strength of the net field is fixed by the initial beta, $\beta = 200$. The corresponding Alfvén length is then $l_A = \sqrt{2/\beta}H_0$, which is roughly 3 times Δ. Thus the input scale of the MRI turbulence is resolved, but there is no inertial range to speak of — a serious deficiency of our, and most extant, MRI simulations (but see Fromang 2010 and Meheut et al. 2015).

Turbulence in net-toroidal simulations develops slowly, over tens of orbits, irrespective of the temperature increase.
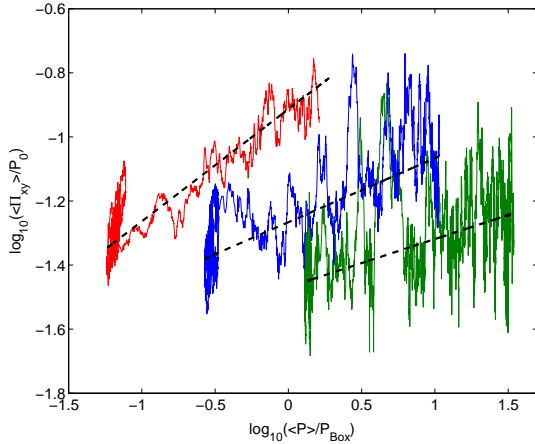
Figure 9. The time evolution of the total stress normalized by the initial gas pressure, as a function of the volume averaged pressure for the net-toroidal simulations with $L = 4H_0$ (red curve), $L = 2H_0$ (blue curve) and $L = H_0$ (green curve). The superimposed lines have slopes $0.15, 0.2, 0.35$.

β	v_A	$\langle \Pi_{xy} \rangle / P_0$	q
50	0.200	0.098	0.1-0.2
200	0.100	0.051	0.3-0.4
500	0.063	0.033	0.4-0.5
5000	0.020	0.024	0.4-0.5
10^4	0.014	0.025	0.4-0.5

Table II. Average total stresses calculated in the initial thermal equilibrium of the net toroidal simulations described in Section 5.1.1. as well as estimated q values using these states as restarts.

Figure 10. Stress against pressure for $L_z = 4H_0$ net-toroidal simulations with $\beta = 50$, 2×10^2 and 10^4 (red, green, and blue respectively). Dashed lines with slopes 0.15, 0.35 and 0.4 have been superimposed (in descending order).

This initial phase complicates the interpretation of the stress's growth and makes attributing a well-defined q problematic. In order to oversome this obstacle, we remove the slow non-linear development of the turbulence. Our strategy is to introduce cooling at the beginning of the run and let the box come to thermal equilibrium with a quasi-steady H near a target H_0. The cooling function adopted is $\Lambda = \theta P^2$. Once the system has remained in this quasi thermal equilibrium for ~ 30 orbits the cooling is removed and the pressure allowed to increase. Subsequently, any increase in stress will be due to the change in pressure alone and not due to the initial long transient.

Results from these simulations are shown in Fig. 9. We find that q increases with box size, from ≈ 0.15 in the $L = H_0$ simulation to ≈ 0.35 in the $L = 4H_0$. The stress-pressure relationship is weaker than for the zero-net-flux case, but we can still discern the influence of the box size in limiting q. It is unclear, however, if q has converged yet with respect to L.
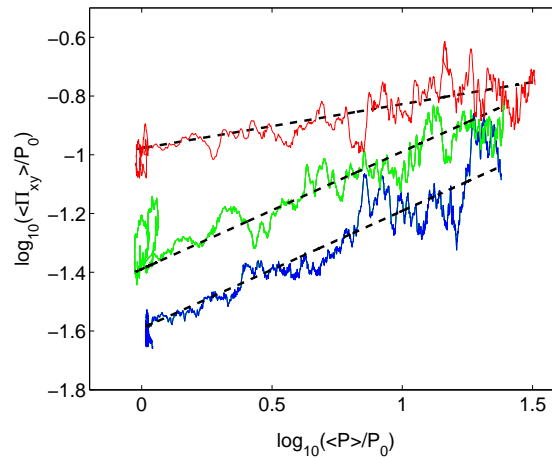
5.1.1 Field strength dependence

The stress in net-flux simulations is not only governed by c_s but also by the strength of the imposed magnetic field. Indeed HGB95 found that $\Pi_{xy} \propto E_B \propto v_A$ in their early net-vertical and net-toroidal flux simulations, where E_B is the total magnetic energy. The same scaling was noted by GGSJ09, who argued that $\Pi_{xy} \propto c_s v_A$. Assuming this holds for thermally evolving systems, this means the stress must be proportional to the square root of P, i.e. $q = 0.5$. The value of q measured in the last subsection is marginally consistent but slightly smaller than this scaling. The difference may be attributed to the remaining influence of the box size, the grid, or the strength of the imposed field, which we explore now.

To study the effect of the imposed flux we perform $L = 4H_0$ simulations with $\Delta = H_0/32$ but with $\beta = 50$, 2×10^2, 5×10^2, 5×10^3, and 10^4. We first let the simulations

settle into a thermal equilibrium before setting $\Lambda = 0$ and letting them heat up.

Firstly, during the thermal equilibrium stage when P is quasi-steady, we find that $\Pi_{xy} \propto v_A$ if $l_A > \Delta$, Table II. Thus our diabatic equilibrium simulations agree with previous isothermal runs (GGSJ09) and heating runs (HGB95). Note that when the magnetic tension is not resolved, $l_A < \Delta$, the average stress becomes independent of field strength.

Secondly, during the heating phase of the simulations, we find that the stress-pressure relationship also depends on v_A. Our results are shown in Fig. 10, which reveal that q is an increasing function of β. For our moderate strength toroidal fields simulations, $\beta = 200, 500$, we obtain $q \approx 0.35$. Increasing the field strength decreases q to $0.15 - 0.2$, while for our weak field simulations $q = 0.35 - 0.5$.

The weak field runs are easy to understand: the Alfvén length, l_A, is less than the grid Δ. Consequently, the fluid barely 'feels' the magnetic tension from the imposed field and instead behaves as if the box were zero-net flux. This explains the larger q for the $\beta = 2 \times 10^2$ and 10^4 simulations, which approach the results of Section 4.1.

When l_A is resolved, the reason for the weaker dependence of stress on pressure is more difficult to attribute. One idea is the following: low β simulations exhibit rapid heating, the speed of which could outstrip the ability of the fluid to adjust to the rising temperature. As a result, the stress-pressure relationship could be weakened. To test this we slow down the heating via a cooling law that is precisely half the heating rate, i.e. $\Lambda = \frac{1}{2} dP/dt$. The result is plot-
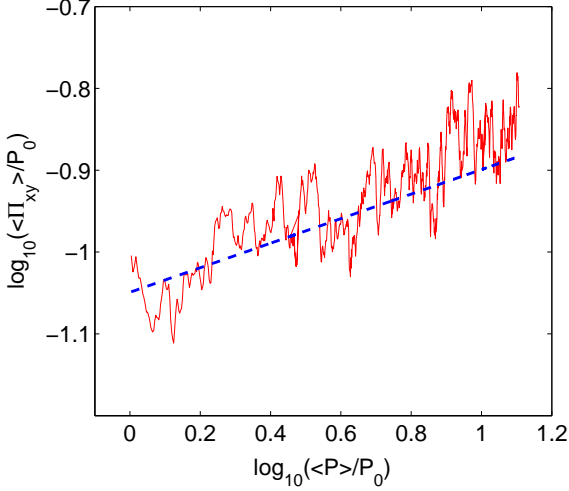
Figure 11. Stress against pressure for the $L = 2H_0$ net-toroidal simulations with $\beta = 50$ and reduced heating. The dashed line has slope 0.15.

Figure 12. Total stress, normalised by the pressure, as a function of the ratio of the box size to scale height for isothermal net-toroidal simulations. For comparison, a curve with $\alpha \propto (L/H_0)^{0.45}$ is overlaid.

ted in Fig. 11, where we see no change in the measured q. Thus very fast heating is not the culprit in the low-β low-q connection.

Could the weak dependence be a result of a too-small azimuthal box size? GGSG09 show that the longest horizontal correlation lengths are less than H in isothermal simulations with $\beta = 100$ and 400. This suggests that even at $\beta = 50$ the turbulence is unrestrained by the domain's azimuthal size. To check, however, we undertook a simulation with $L_x = L_z = 4H_0$, $L_y = 10H_0$, and $\beta = 50$. The measured q is little different to the smaller box with the maximum horizontal correlation length $\lesssim H$.

The most likely explanation, perhaps, is that a strong imposed magnetic field interferes with the manner in which acoustic radiation limits the flow, possibly by altering the nature of the pressure waves or by directly impeding the turbulent motions themselves. Magnetic tension may not only enable the MRI but also restrict its nonlinear development, especially on smaller scales. Dedicated simulations could help test and further develop this idea.

5.1.2 Isothermal runs

For completeness we also performed a number of isothermal simulations, identical to the second set of simulations of Section 4.3 (where the number of grid points per H is kept constant) but with net toroidal magnetic flux and $\beta = 1000$. The simulations are summarised in Table I.

This sequence yields approximately the same relation between saturated stress and box size as in zero-net flux simulations, $\Pi_{xy} \sim (L/H)^{2/5}$, plotted in Fig. 12. On dimensional grounds, Π_{xy} must also be proportional to a function of both β and H/Δ. Its β dependence can be constrained by two GGSJ09 simulations at $\beta = 100$ and 400, which show that the stress is $\sim \beta^{-1/2}$. For this range of magnetic field strength we then have

$$\Pi_{xy} \sim \rho v_A \, L^{2/5} H^{3/5} \Omega \, f(H/\Delta), \qquad (17)$$

where f is a dimensionless function. GGSJ09 also conduct a
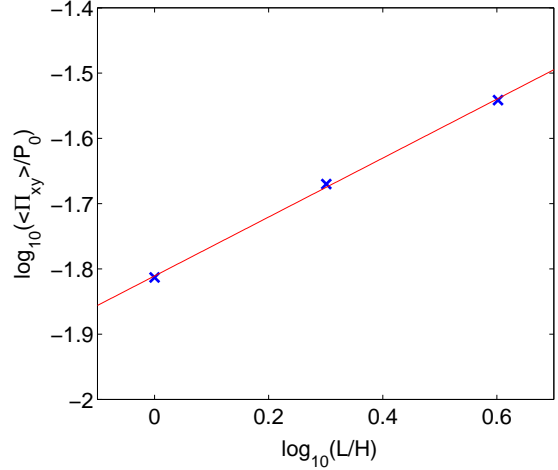
resolution study and argue that once l_A is resolved the magnetic energy (and consequently, stress) becomes independent of resolution. If true, then f is approximately a constant and Eq. (17) yields $q = 0.3$, in reasonable agreement with the heating runs of Section 5.1, for similar β.

Obviously, when the magnetic field is stronger the scaling breaks down, and the H dependence must diminish. On the other hand, for weaker fields (when l_A approaches and then slips below Δ) the v_A dependence weakens. A more comprehensive set of simulations probing a wider range of field strengths and resolutions may better constrain the behaviour of Π_{xy}.

5.2 Vertical fields

Finally, we undertake a set of simulations with a net-vertical-flux penetrating the computational domain. Our aim is to augment the main trends of previous sections, rather than to be comprehensive. The main result here is that $\Pi_{xy} \sim P^{1/2}$ in boxes of larger vertical extent, and for weaker magnetic fields.

Simulation domains with a greater than unity aspect ratio, the ratio of the radial to vertical lengths, exhibit diminished channel modes (Bodo et al 2008). As channel bursts distort the stress-pressure relation, we always use an appropriate aspect ratio $L_x/L_z = 2$ to minimize their influence. We first take a box of size $(2H_0, 5H_0, H_0)$ with $\Delta = H_0/64$ and set $\beta = 1000$. The resulting relation that we obtain is very weak, $q = 0 - 0.15$. We believe this to be in agreement with SITS04, who find $q = 0.17$, HGB95 and SHB09 who find no relation between stress and pressure, and MHS15 who find a weak correlation or no relation at all depending on the numerical scheme.

Increasing the box size to $(4H_0, 5H_0, 2H_0)$ leads to extremely rapid heating and the scale height exceeds the box size within a few orbits. Disentangling initial growth from the pressure dependence is impossible and therefore we introduce a cooling function, as in Section 5.1.1, to slow the heating: Λ is set to $1/2$ the heating rate. We also reduce the
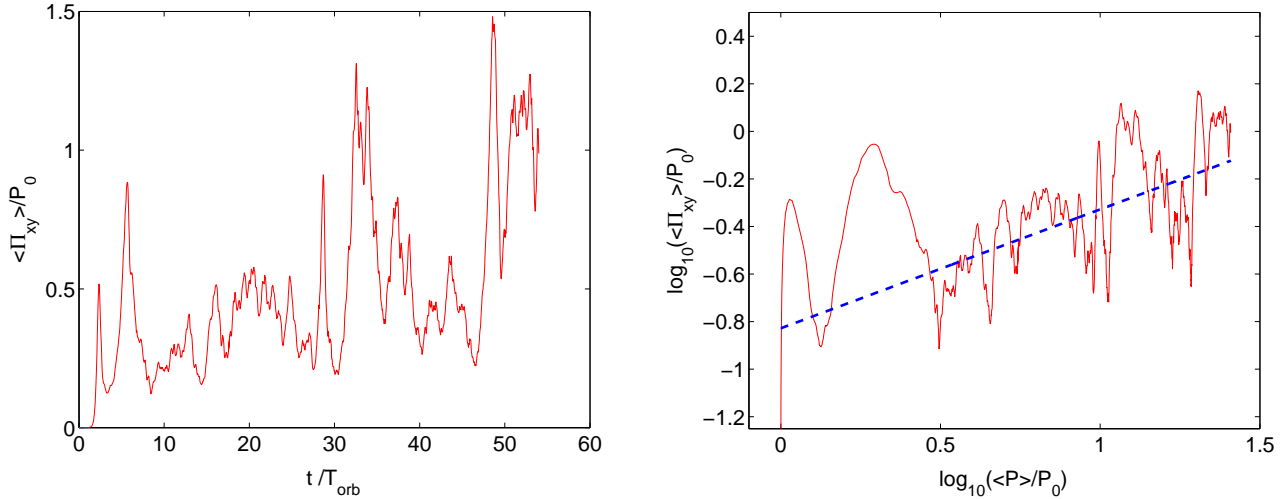
Figure 13. The time evolution of the total stress normalized by the initial gas pressure for the $(4H_0, 5H_0, 2H_0)$ simulation with resolution $\Delta = 1/32$, $\beta = 500$ and reduced heating. The left panel shows Π_{xy} as a function of time, the right panel as a function of P. The dashed line has $q = 0.5$.
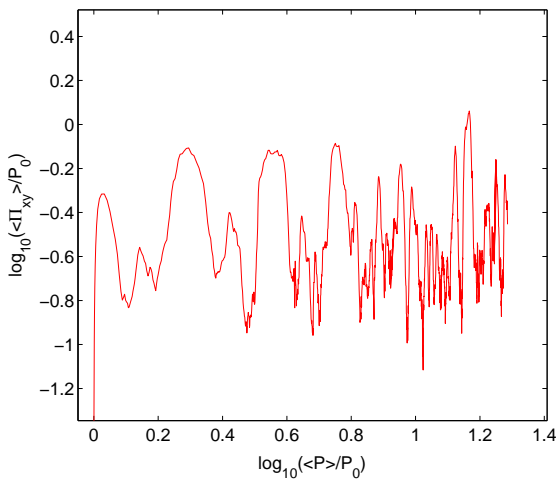
Figure 14. The time evolution of the total stress normalized by the initial gas pressure, as a function of the volume averaged pressure for the $(2H_0, 5H_0, H_0)$ simulation with $\Delta = 1/32$, $\beta = 500$ and reduced heating. The plot should be compared with the right panel of Fig. 13.

resolution to $H_0/32$ and, to compensate, we increase the field strength so that $\beta = 500$. The evolution of the simulation is shown in Fig. 13. After two initial channel spikes there is an increase in stress with pressure over the next 50 orbits with approximately $q \approx 0.5$, a remarkable contrast to the smaller box. For direct comparison, we plot, in Fig. 14, log P against log Π_{xy} from a smaller simulation of $(2H_0, 5H_0, H_0)$ with identical cooling, resolution and β. Again, there is little to no correlation between stress and pressure.

In principle, one could explore the connection between q and β. But decreasing β further leads to more prominent channel activity because the system is closer to criticality; these bursts complicate the heating and stress behaviour and hence the extraction of a reliable q. Lower β s require larger L_x and L_y, and more computationally expensive runs

as a result. We leave open the question of the β dependence of q to future work, but expect similar outcomes to Section 5.1.

6 DISCUSSION AND CONCLUSION

The main aim of our paper is to highlight the importance of box size in the relationship between MRI-induced stress and pressure. In most previous simulations the pressure scale height H was greater than the vertical size of the computational domain L. Consequently, turbulent eddies were not restricted by the compressibility effects assumed by the alpha model, and so the associated stresses were unable to manifest a meaningful dependence on pressure.

In order to bring out the true relationship between Π_{xy} and P we present simulations in the opposite regime, when $H < L$. Generally, we find a stronger dependence, and in zero-net flux simulations with explicit diffusivities we almost reproduce $\Pi_{xy} \propto P$, as required by the α-disk model. The same simulations without explicit diffusivities, however, cannot escape the influence of the grid and remain unconverged with respect to the numerical parameters.

Toroidal-net-flux simulations witness a weakening of the stress-pressure relationship once the imposed magnetic field gets too large. It is possible that this is to do with enhanced magnetic tension, and consequently a greater proximity of the MRI to criticality, though how this works out physically is unclear. Weaker fields in both net-toroidal and vertical runs ($\beta > 100$) roughly suggest the scaling $\Pi_{xy} \lesssim c_s v_A$, which is consistent with GGSJ09, though its origin is also mysterious and the role of numerical factors is still to be fully determined.

Our results present various puzzles and problems that future simulations should pursue. Further work is required to understand the zero-net-flux simulations with explicit diffusivities. In particular, why does the growth in Π_{xy} halt 'prematurely'? Simulations in large boxes and different Reynolds numbers may help probe this behaviour. Other

angles to take include potential Prandtl number or box aspect ratio dependencies. Our toroidal flux simulations omit explicit diffusivities but it would be beneficial to see what changes occur, especially in q, when they are present. In the strong field, low β, regime the adjustment should be marginal. For weaker fields, when the Alfvén length is small, we anticipate more noticeable discrepancies. The q-β connection in vertical-flux simulations could also be explored more fully. Finally, it would be beneficial to extend our isothermal simulations. Of most interest would be zero-flux runs with explicit diffusion, and toroidal-flux runs exploring different β.

An obvious generalisation of this work would be to include vertical stratification. Unstratified boxes can cleanly test the most fundamental idea of the alpha model: that acoustic radiation limits the development of disk turbulence. However, when $L > H$, the vertical structure of the disk should really be included. Pressure controls the disk thickness and this geometric effect (omitted in unstratified boxes) presents a second way that pressure may influence Π_{xy}. Future work in this direction is challenging. In zero-net-flux simulations it may be difficult to escape the influence of the grid, due to resolution constraints. Net-vertical flux simulations, on the other hand, may be complicated by the emergence of outflows (Fromang et al. 2013, Bai & Stone 2013, Lesur et al. 2013).

We finish with a short discussion on thermal instability in accretion disks, the main impetus for this work. Essentially, thermal instability must rely on the competing dependencies of the heating and cooling on temperature. To establish stability or instability we then must have knowledge of how Π_{xy} depends on pressure. The classical instability of radiation-pressure dominated accretion flows assumes that the stress is proportional to total pressure (Lightman & Eardley 1974, Shakura & Sunyaev 1976, Piran 1978). Of course, radiation pressure is omitted in our simulations, but a useful first step is to establish how Π_{xy} depends on gas pressure alone and to highlight constraints on the stress's evolution. This may then aid in the interpretation of more advanced simulations, especially as they appear to produce contradictory stability behaviour (Hirose et al. 2009, Jiang & Stone 2013). In particular, divergent results are obtained in boxes of different L_x. A natural question is: does the stability's box-size dependence issue from the kind of variable stress-pressure relationship explored in our paper? Another question is: how captive are these stability results to the numerical parameters, in particular the grid scale Δ? As shown in zero-net-flux runs, the stress is propotional to Δ hence weakening its dependence on P and denying it numerical convergence. In the light of that, how are we to interpret these simulations and then apply them to real systems?

ACKNOWLEDGMENTS

REFERENCES

Bodo. G., Mignone. A., Cattaneo. F., Rossi. P., Ferrai. A., 2008, A&A, 487, 1.

Bai. X-N., Stone. J. M., 2013, ApJ, 767, 30.

Balbus. S. A., Hawley, J. F., 1991, ApJ, 376, 214-233.

Balbus. S. A., Hawley. J. F., 1998, Rev. Mod. Phy., 70, 1.

Blackman. E. G., Penna. R. F., Varnire. P., 2008, New Astronomy, 13, 224-251.

Fromang. F., A&A, 2010.

Fromang. S., Hennebelle. P., Teyssier. R., A&A, 2006, 457, 371-384.

Fromang S., Latter H., Lesur G., & Ogilvie G. I., 2013, A&A, 552, A71

Fromang. S., Papaloizou. J., A&A, 2007, 476, 1113-1122.

Fromang. S., Papaloizou. J., Lesur. G., Heinemann. T., A&A, 2007, 476, 1123-1132.

Fromang. S., Stone. J., 2009, A&A, 2009, 28, 19-28.

Goldreich. P., Lynden-Bell., MNRAS, 1965, 130, 125

Goodman. J., Xu. G., ApJ, 1994, 432, 213-223.

Guan. X., Gammie. C. F., Simon. J. B., Johnson. B. M., 2009, ApJ, 694, 1010-1018.

Hawley. J. F., Gammie. C. F., Balbus. S. A., 1995, ApJ, 440, 272.

Hirose. S., Krolik. J. H., Blaes. O, 2009, ApJ, 691, 16-31.

Jiang. Y., Stone. S. M., Davis. S. W., 2013, ApJ, 778, 65

Latter. H., Lesaffre. P., Balbus. S. A., MNRAS, 2009, 394, 715-729.

Latter. H. N., Fromang. S. & Gressel. O, 2010, MNRAS, 406, 848.

Latter. H. N., Papaloizou. J. C. B., 2012, MNRAS, 426, 1107-1120.

Lesaffre. P., Balbus. S. A., Latter. H., MNRAS, 2009, 396, 779-787.

Lesur. G., Ferreria. J., Ogilvie. G. I., 2013, A&A, 550, A61.

Lesur. G., Longaretti. P.,MNRAS, 2007, 378, 1471.

Lightman. A. P., Eardley. D. M., 1974, ApJ, 187, L1-L3.

Lynden-Bell, D., Pringle, J. E., 1974, MNRAS, 168, 603-637.

Meheut. H., Fromang. S., Lesur. G., Joos., Longaretti. P., 2015., A&A

Minoshima. T., Hirose. S., Sano. T., 2015, preprint (arXiv:1506.03524)

Miyoshi. T., & Kusano. K., 2005, J. Comput. Phys., 208, 315

Ogilvie. G. I., 2003, MNRAS, 340, 969-982.

Pessah. M., Chan. C., Psaltis, D., 2006, MNRAS , 372, 183-190.

Pessah. M., Chan. C., and Psaltis. D., 2007, MNRAS, 372, 183-190.

Pessah. M. E., Goodman. J., Ap. J. L., 2009, 698, L72-L76.

Piran. T., 1978, ApJ, 221, 652-660.

Riols. A., Rincon. F., Cossu. C., Lesur. G., Longaretti. P. Y., Ogilvie. G. I., Herault. J., Journal of Fluid Mechanics, 2013, 731, 1-45.

Riols. A., Rincon. F., Cossu. C., Lesur. G., Longaretti. P. Y., Ogilvie. G. I., Herault. J., A&A, 2015, 575, A14.

Sano. T., Inutsuka. S., 2001, ApJ, 561, L179-L182.

Sano, T., Inutsuka, S and Turner, N. J., Stone, J, M., 2004. ApJ, 605, 321.

Shakura. N, Sunyaev. R., 1973, A&A, 24, 337-355.

Shakura. N, Sunyaev. R., 1976, MNRAS, 175, 613-632.
Simon. J. B., Hawley. J. F., Beckwith. K., 2009. ApJ, 690, 974.
Stone. J., Gardiner. T., ApJSS, 2010, 189, 142-155.
Suresh. A., 2000, SIAM J. Sci. Comp., 22, 1184
Teyssier. R., 2002, A&A, 364, 337-364.

APPENDIX A: NUMERICAL TESTS

In this appendix, we describe several numerical tests that have been performed to check the implementation in the code RAMSES of the shearing box source terms in the energy equation. A satisfactory second order convergence was obtained in all of these tests.

A1   Shearing waves

In order to test the implementation of azimuthal advection, we have performed numerical simulations of two types of particularly simple shearing waves. The first exhibits an azimuthally varying entropy and density but uniform pressure:

$$\rho = \rho_0 \left[1 + A \cos \left(\frac{2\pi n_y y}{L_y} \right) \right], \tag{A1}$$

$$P = P_0, \tag{A2}$$

where ρ_0, and P_0 are the background density and pressure, A is a dimensionless amplitude of the entropy wave, n_y the number of wavelengths in the azimuthal size of the box L_y. The second possesses an azimuthally varying vertical magnetic field strength, but uniform entropy and total pressure (including magnetic pressure):

$$\rho = \rho_0 \left[1 + A \cos \left(\frac{2\pi n_y y}{L_y} \right) \right], \tag{A3}$$

$$B_z^2 = B_0^2 - 2P_0 \left[\left(\frac{\rho}{\rho_0} \right)^\gamma - 1 \right], \tag{A4}$$

$$c_s^2 = c_{s0}^2 \left(\frac{\rho}{\rho_0} \right)^{\gamma-1}, \tag{A5}$$

where B_0 is the background vertical magnetic field strength, c_s is the sound speed, c_{s0} its background value.

These two types of waves are simply advected by the flow, and therefore sheared, without inducing any movement or pressure perturbation. The analytical solution of the time-evolution of the these waves is particularly simple

$$f(x, y, t) = f(x, y + xSt, 0) \tag{A6}$$

where f is any physical quantity, S is the shearing rate.

We have performed two-dimensional simulations (in the x-y plane) of both types of waves, with fiducial parameters $L_x = 1$, $L_y = 4$, $A = 10^{-3}$, $n_y = 1$, $\gamma = 1.4$, $\rho_0 = 1$, $c_{s0} = 1$, $\Omega = 1$. We used various radial resolutions, $\Delta = 1/20, 1/40, 1/80, 1/160$ with the azimuthal grid size twice the radial in each case. Fig. A1 shows the distribution of sound speed one orbit after the beginning of the simulation of the magnetic shearing wave with $n = 2$. Fig. A2 shows the L1 norm of the deviation from the analytical solution for the density (black) and the total pressure (red) as a function of resolution. The convergence is quadratic as expected for a second order code. In the case of the entropy wave, we obtain a similar convergence of the error on the density distribution. Pressure and velocity perturbations are
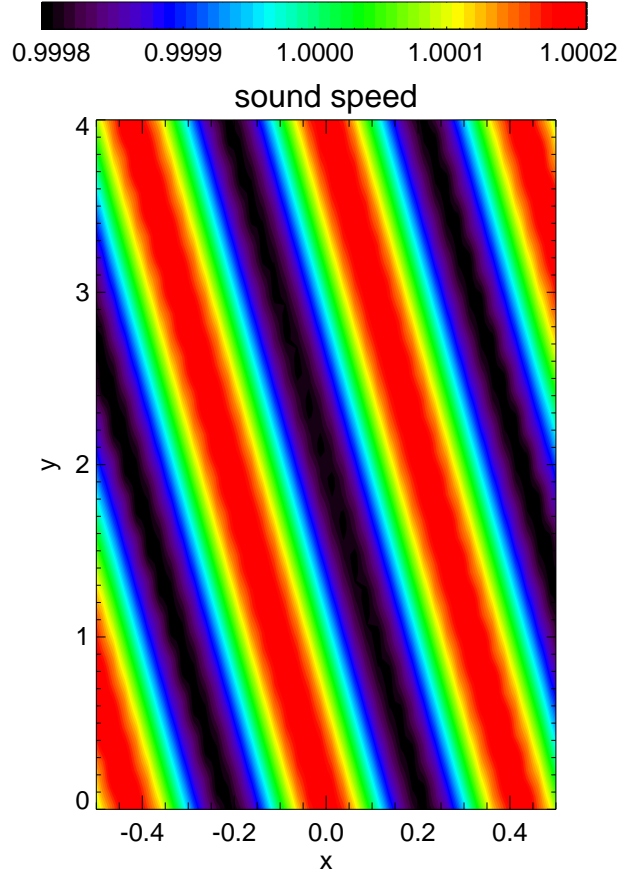
Figure A1. Sound speed distribution after one orbit of evolution for the magnetic shearing wave.
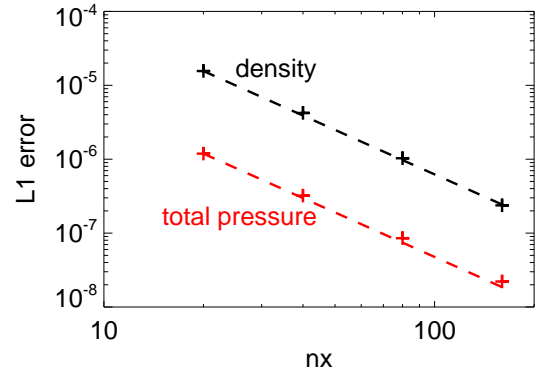
Figure A2. Error on the density (black) and total pressure (red) after one orbit of evolution for the magnetic shearing wave.

induced only at truncation error, likely because the pressure, and therefore energy E', is uniform in the box.

A2   Epicyclic oscillations

A basic test of the implementation of the shearing box source terms is epicyclic oscillations. We initiate epicyclic oscillations of a shearing box with uniform density and pressure by

setting the radial velocity to a uniform and constant value $v_0 = c_s$. For the momentum evolution, we obtain very similar results to Stone & Gardiner (2010): the energy of the epicyclic oscillations $E_{\text{epi}} = 0.5\rho \left(v_x^2 + 4v_y'^2 \right)$ is conserved to truncation error, as expected since we use the same Crank-Nicholson algorithm, while a small dispersion error is observed at low resolution. The pressure remains at its initial value, up to truncation error, which shows that the source term in the energy equation involving the Reynolds stress is accurately computed.

We also considered epicyclic oscillations in a radially non-uniform box, containing a radially varying entropy wave with uniform pressure as

$$\rho = \rho_0 \left[1 + A \cos \left(\frac{2\pi n_x x}{L_x} \right) \right], \tag{A7}$$

$$P = P_0, \tag{A8}$$

where n_x is the number of wavelengths in the radial extent of the box. We performed one dimensional simulations with the following parameters : $L_x = 1$, $v_x = c_{s0}$, $c_{s0} = 1$, $A = 10^{-3}$ and a number of grid points varying between 20 and 160. In this case, numerical errors induce pressure perturbations, which converge quadratically.

## APPENDIX B: ROBUSTNESS OF RESULTS ON NUMERICAL PARAMETERS AND SET UP

In this appendix we present some ancillary simulations to Sections 4 and 5 showing the robustness of the main results. In the main body of the text we examine the effect of resolution and explicit diffusion. Here we test initial conditions and confirm that our choice of resolution is adequate when using explicit diffusion coefficients.

B1   Initial conditions

In Section 4 we consider zero-net-flux systems that are out of equilibrium and evolving with time. The phenomena that we are primarily interested in occur relatively early in the simulations and so the initial conditions may not have been completely forgotten and may be influencing our results. We check how robust they are to the choice of initial condition. Instead of small amplitude noise we use as an initial condition a turbulent quasi-equilibrium. To generate this quasi-equilibrium we used the same computational set-up as the fiducial $L = 2H_0$ zero-net-flux simulation but we introduce a cooling law $\Lambda = \theta P^2$ into the energy equation. This prescription ensured a stable non-zero thermal equilibrium point from which we could restart the simulation with out any cooling. The results are shown in Fig. B1 and show the increase in stress with pressure with a comparable q to our fiducial simulation, $q = 0.35 - 0.65$.

B2   Dissipation

In Section 4.1.2 we perform simulations with explicit diffusion and resistivity accounted for with $Re = 1250$ and $R_m = 5000$ and with a grid of $\Delta = 1/64$. It is necessary to check that the grid is sufficient small to ensure negligible numerical diffusion and dissipation. Our approach was to
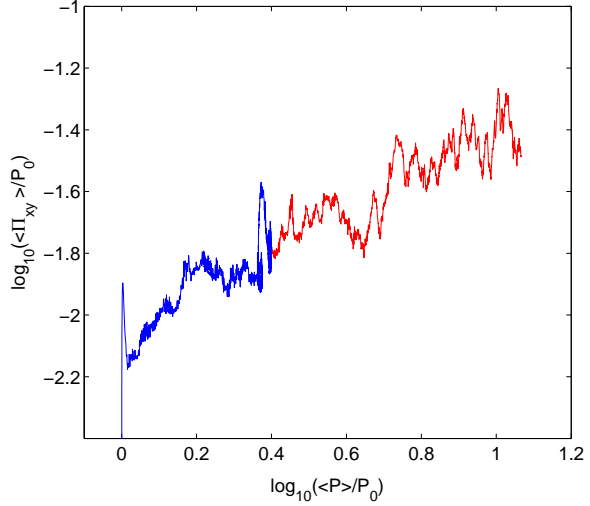
Figure B1. The time evolution of the Maxwell stress normalized by the initial gas pressure, as a function of the volume averaged pressure for $L = 2H_0$ simulations. The blue curve is from the simulation bringing the system to a thermal equilibrium and the red curve is when the cooling is removed.

consider the contributions to the volume averaged internal energy $\langle \epsilon \rangle$. The rate of change in $\langle \epsilon \rangle$ can be written as

$$\langle \dot{\epsilon} \rangle = -\langle P \nabla \cdot \mathbf{v} \rangle + \langle D_{\text{phy}} \rangle + \langle D_{\text{num}} \rangle \tag{B1}$$

where $\langle D_{\text{phy}} \rangle$ and $\langle D_{\text{num}} \rangle$ are the volume averaged contributions from physical and numerical dissipations respectively.

For our choice of parameters to be appropriate we must have $\langle D_{\text{num}} \rangle < \langle D_{\text{phy}} \rangle$. We compute these quantities for a $L = H_0$ zero net-flux box with the above choice of parameters. These box averaged quantities are plotted in Fig. B2. This shows that the total time averaged numerical diffusion is significantly less than the total physical dissipation but roughly equal to the (subdominant) viscous dissipation.

To further check that a resolution of $\Delta = 1/64$ gives appropriate results for our chosen Re and R_m, we undertook $L = 2H_0$ heating simulations with $\Delta = 1/64$ and $1/128$. Both yielded $q \approx 0.5$ and a maximum stress that was roughly consistent.
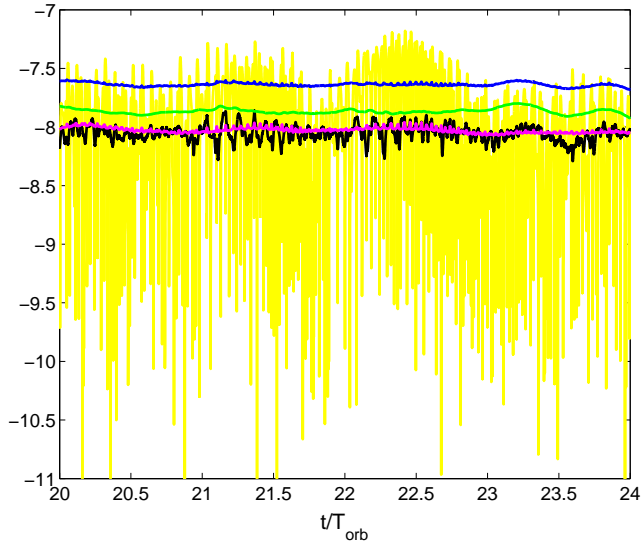
Figure B2. Various box-averaged thermal energy input terms plotted on a log_{10} scale over 4 orbits. The green curve is the Ohmic heating, pink is the viscous heating, blue is the sum of the Ohmic and the viscous heating, yellow is the pressure heating term and the black curve is the numerical heating.